Supplement of The Cryosphere, 14, 1459–1474, 2020
https://doi.org/10.5194/tc-14-1459-2020-supplement


The Cryosphere
Open Access

*Supplement of*

# Spatial probabilistic calibration of a high-resolution Amundsen Sea Embayment ice sheet model with satellite altimeter data

**Andreas Wernecke et al.**

*Correspondence to:* Andreas Wernecke (andreas.wernecke@open.ac.uk)

## S1 Typical correlation length scale of ice thickness change

Using the seven year mean, gridded (10 km$\times$10 km) $dh/dt$ data from Konrad et al. (2017) for the ASE we derived a semivariogram (Figure S1) which has a range value for the shown exponential fit of approximately 28000 m. Therefore the covariance of measurements 28 km apart from each other reaches only about 63% of the far field variance (the sill$=$ 2 m$^2$ a$^{-2}$). This is in agreement with visual inspections for Figure 1 of Konrad et al. (2017) and means that neighbouring grid cells on the used resolutions can in deed not be considered independent.

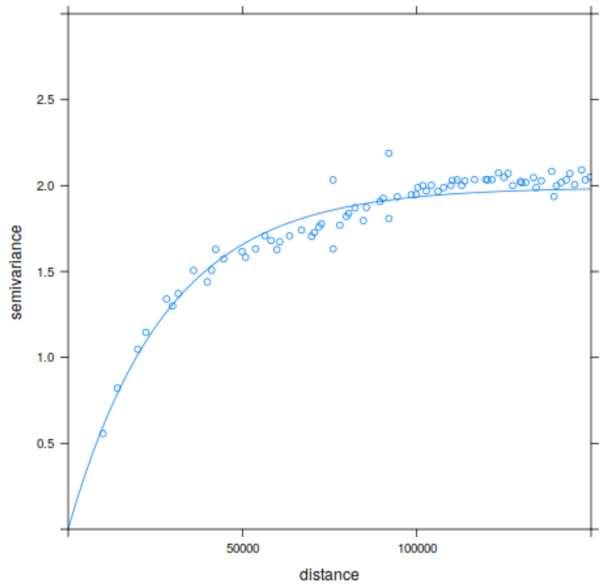


**Figure S1.** Semivariogram of ice thickness change in the Amundsen Sea sector based on observations from Konrad et al. (2017)

## S2 Synthetic experiment tests

Figure S2 and S3 show a variety of synthetic test cases for calibration in basis representation, as described in the main manuscript.

### S2.1 Central runs with different bedrock and sliding laws

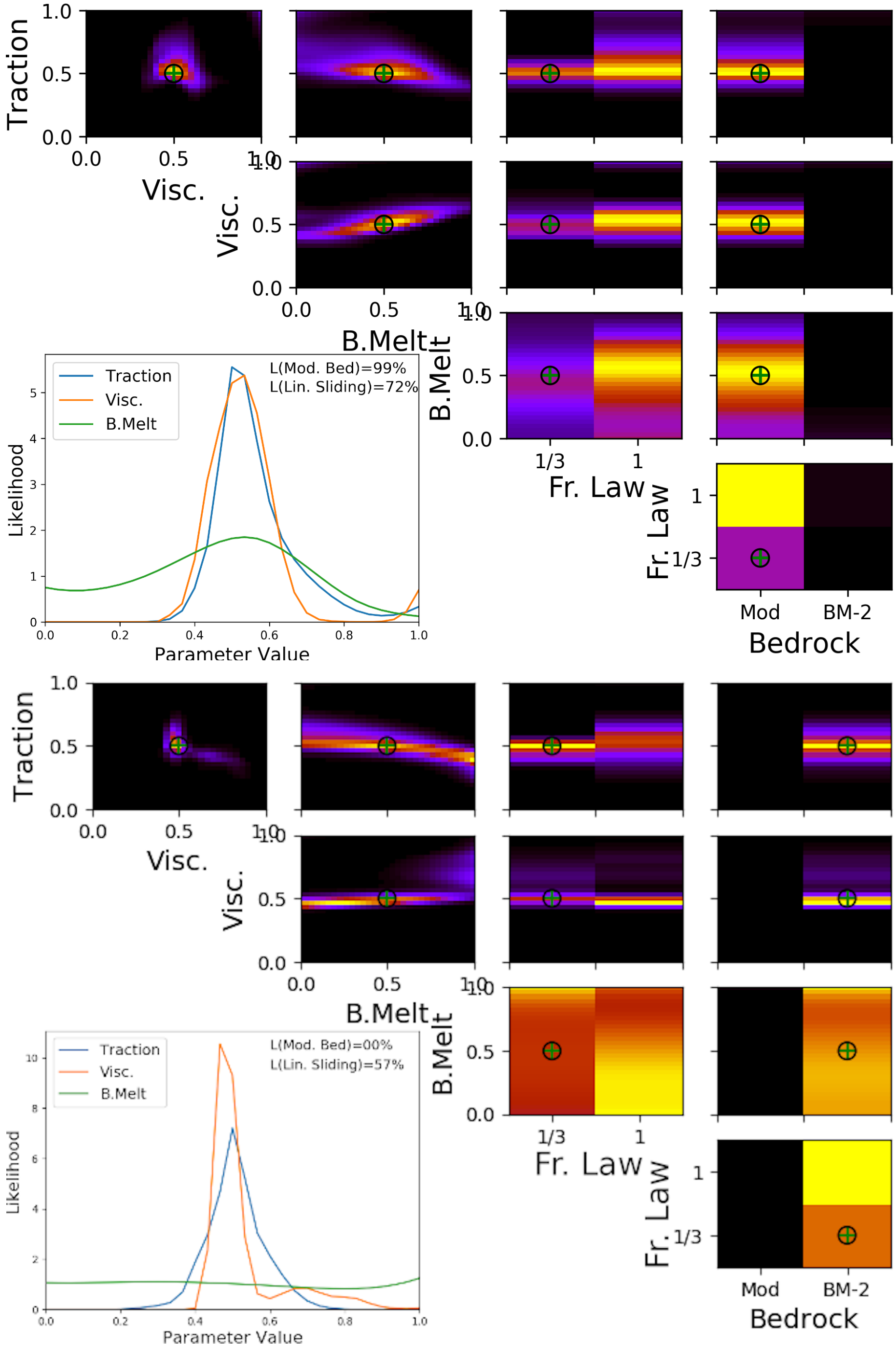


**Figure S2.** Likelihood of parameter combinations of synthetic test case (evaluations of Equation 12). Upper right panels show likelihood values marginalized to pairs of parameters, normalized to the respective maximum for clarity. Lower left panel shows likelihood values marginalized to individual parameters for the three scalar parameters (line plots), and sliding law and bedrock topography map (text and quotation within), normalized to an integral of one, consistent with Probability Density Functions. The central values for traction, viscosity and ocean melt as well as nonlinear sliding are used. The parameter values are also shown by the black circles, while the values of the set of parameters with highest likelihood are shown by green crosses.

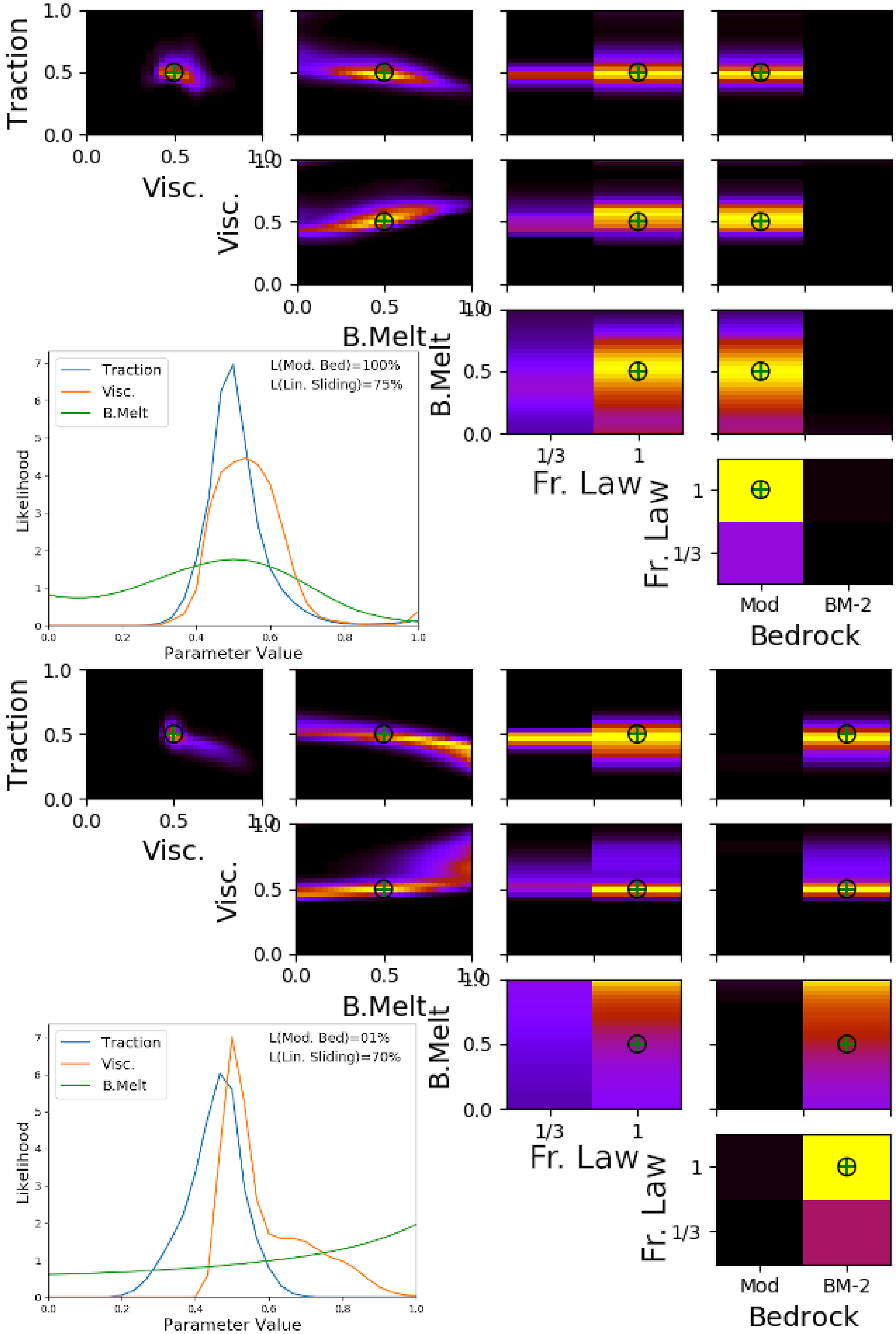


**Figure S3.** Likelihood of parameter combinations of synthetic test case (evaluations of Equation 12). Upper right panels show likelihood values marginalized to pairs of parameters, normalized to the respective maximum for clarity. Lower left panel shows likelihood values marginalized to individual parameters for the three scalar parameters (line plots), and sliding law and bedrock topography map (text and quotation within), normalized to an integral of one, consistent with Probability Density Functions. The central values for traction, viscosity and ocean melt as well as linear sliding are used. The parameter values are also shown by the black circles, while the values of the set of parameters with highest likelihood are shown by green crosses.

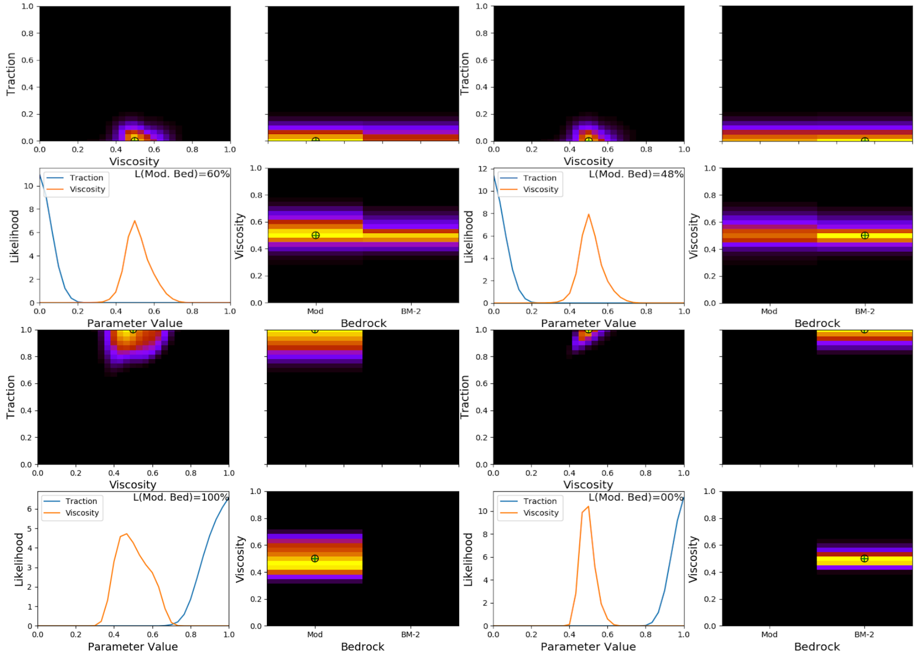


**Figure S4.** Likelihood of parameter combinations of synthetic test case (evaluations of Equation 12). Upper right panels show likelihood values marginalized to pairs of parameters, normalized to the respective maximum for clarity. Lower left panel shows likelihood values marginalized to individual parameters for traction and viscosity parameters (line plots), and bedrock topography map (text and quotation within), normalized to an integral of one, consistent with Probability Density Functions. The synthetic test values for traction, viscosity and bedrock are shown by the black circles, while the ocean melt is 0.5 and nonlinear sliding is used. The set of parameters with highest likelihood are shown by green crosses.

## S2.2 Extreme traction and viscosity values

Figure S4 and S5 show synthetic test cases with priors set to a sliding law exponent $m = 1/3$ and uniform ocean melt, as described in the manuscript.

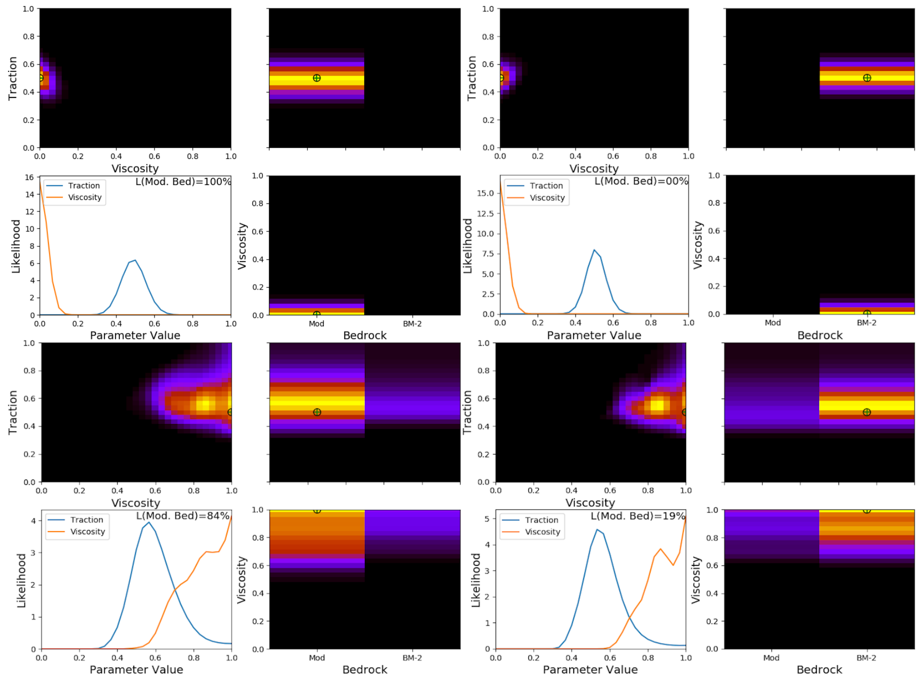


**Figure S5.** Likelihood of parameter combinations of synthetic test case (evaluations of Equation 12). Upper right panels show likelihood values marginalized to pairs of parameters, normalized to the respective maximum for clarity. Lower left panel shows likelihood values marginalized to individual parameters for traction and viscosity parameters (line plots), and bedrock topography map (text and quotation within), normalized to an integral of one, consistent with Probability Density Functions. The synthetic test values for traction, viscosity and bedrock are shown by the black circles, while the ocean melt is 0.5 and nonlinear sliding is used. The set of parameters with highest likelihood are shown by green crosses.

## S2.3 Calibration distribution by sliding law

As can be seen in Figure S6, linear sliding leads to higher frequencies (denser sampling) near the mode (higher peak value) and commonly weaker tails. This explains why, for this test case, linear sliding is attributed higher likelihoods while the test is based on nonlinear sliding.

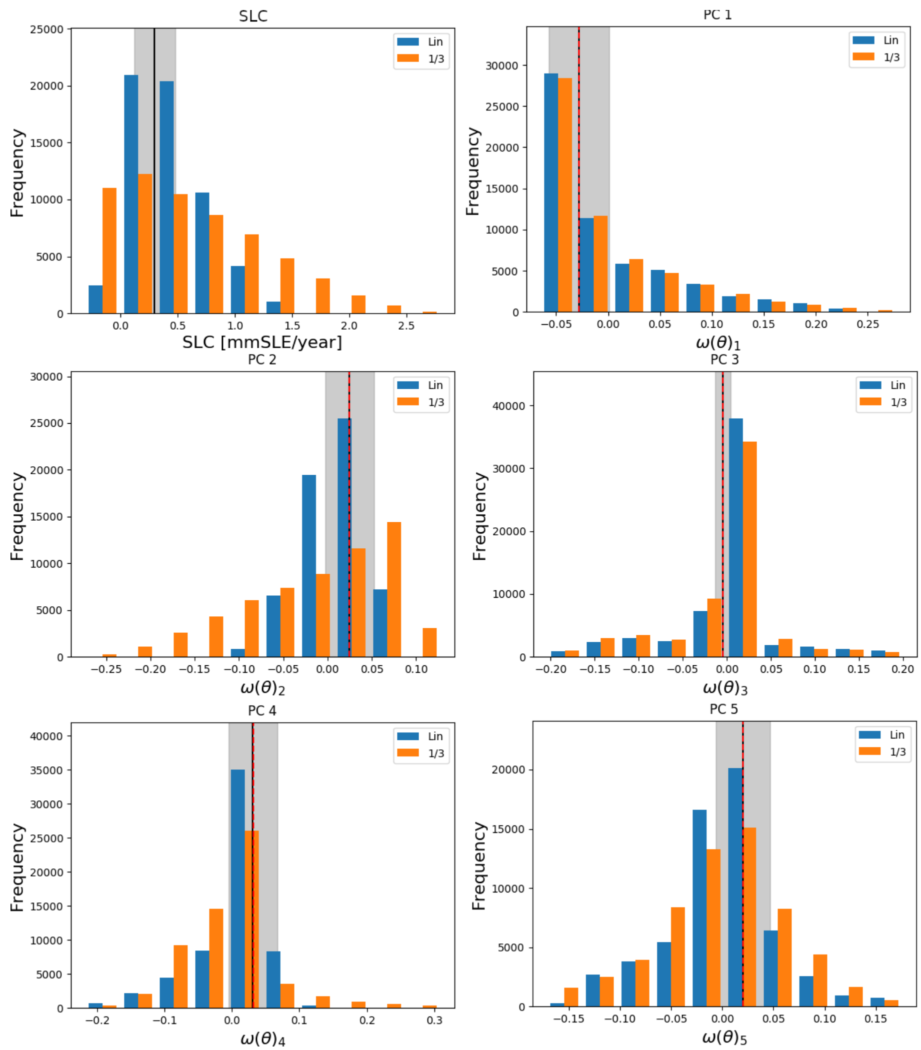


**Figure S6.** Average sea level contribution in calibration period for all emulator calls (upper left) and emulator results ($\omega(\theta)$) for each of the first five PCs, split into linear (blue) and nonlinear (orange). Vertical black lines shows the calibration target ($SLC(\boldsymbol{z_{(xy)}})$ (upper left) and $\hat{z}_{i=1;5}$ (others)) with corresponding $\pm 3\sigma$ interval (shade) and red dashed red lines the correct value from the model run with traction, viscosity, basal melt equal to 0.5 and nonlinear friction plus modified bedrock.

## S3 End-of-simulation likelihood distributions

Figure S7 shows the likelihood distributions for the two alternative calibration approaches.

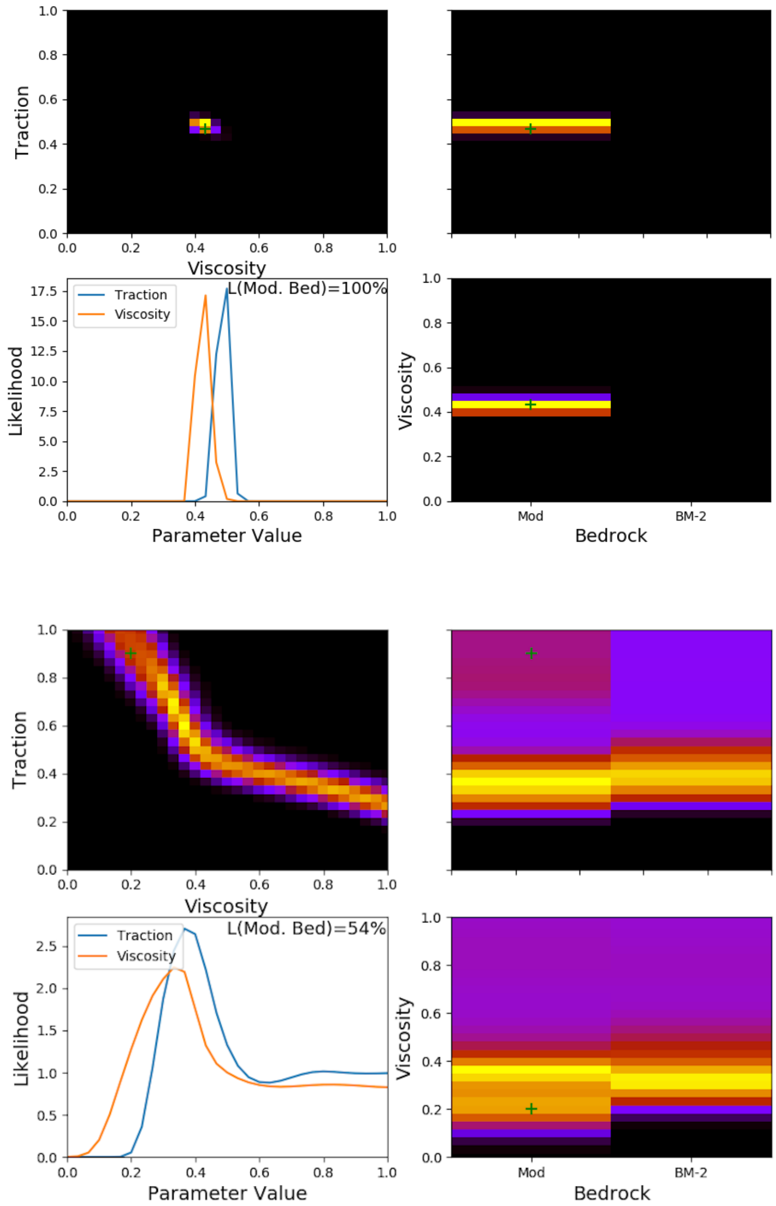


**Figure S7.** Like Figure 5a in the main manuscript but for reprojected $(x, y)$ calibration (top) and SLC calibration (bottom).

**Table S1.** Total sea level contribution after 50 years in mm SLE: (weighted) mean, most likely contribution and percentiles; with and without calibrations.

| | Mean | Mode | 5% | 25% | 50% | 75% | 95% |
|---|---|---|---|---|---|---|---|
| Prior | 30.6 | -3.3 | -8.4 | 4.2 | 23.1 | 51.3 | 94.5 |
| Posterior basis year 1-7 | 19.1 | 18.4 | 13.9 | 16.7 | 18.9 | 21.4 | 24.8 |
| Posterior basis year 1-4 | 21 | 20.2 | 16.8 | 19 | 20.7 | 23 | 25.5 |
| Posterior basis year 4-7 | 19.5 | 18.4 | 15.9 | 17.4 | 19.1 | 21.3 | 24.4 |
| Posterior $(x,y)$ year 1-7 | 19.2 | 18.4 | 16.7 | 17.7 | 18.6 | 21.1 | 22.2 |
| Posterior $(x,y)$ year 1-4 | 27.4 | 27.4 | 27 | 27.4 | 27.4 | 27.8 | 27.8 |
| Posterior $(x,y)$ year 4-7 | 15.7 | 14.8 | 14.4 | 14.5 | 15 | 16.4 | 19.3 |
| Posterior SLC year 1-7 | 16.8 | 17.5 | 7.7 | 13.2 | 16.8 | 20.3 | 25.6 |
| Posterior SLC year 1-4 | 17.5 | 17.5 | 7.8 | 13.8 | 17.5 | 21.2 | 27.3 |
| Posterior SLC year 4-7 | 17.3 | 18.4 | 9.3 | 13.9 | 17.5 | 20.8 | 25 |

## S4 Calibration period

Table S1 shows the influence of the calibration period on posterior distributions for all calibration approaches.

## S5 Emulator regression and validation

We use Gaussian Process (GP) models for emulation and train a separate GP model for each of the five Principal Component (PC) in the calibration period and train a single GP for the total sea level contribution for predictions. We use a Matern ($\frac{5}{2}$) covariance function, with the covariance function (hyper-) parameters being optimized on the marginal likelihood with five repetitions using the Python GPy module. The nugget term is set to zero, forcing the emulator to predict the exact values at training points, reflecting the deterministic nature of the ice sheet model. A constant mean function with $N(0,0.5)$ prior is used, accounting for the initial centering of $\widetilde{\mathbf{Y}}$.

In the following we will illustrate the emulator performance by a leave-one-out (LOO) cross-validation scheme. For this we repeat all steps of the emulator setup for subsets of all but one of the full ensemble, and use that emulator to predict the PC scores of the left-out ensemble member. These are compared with the actual ice sheet model values to validate the emulator. This process is repeated until each ensemble member is left out once.

Figure S8a shows the ice sheet model PC scores versus the LOO emulator prediction of the same quantity. That is: $[\mathbf{S}'\mathbf{V}'^T]_{ij}$ on the x-axis versus $\omega_i(\boldsymbol{\theta_j})_{-j}$ on the y-axis where $\omega_i(\cdot)_{-j}$ is the random distribution mean of the Gaussian Process model for the $i$-th PC trained on all BISILCES runs but $\boldsymbol{\theta_j}$. The error bars represent three STDs of the corresponding emulator uncertainty, $diag(\boldsymbol{\Sigma}_\omega(\boldsymbol{\theta_j})_{-j})_i$ where, again, $_{-j}$ indicates that the emulator training has been done on all runs but $\boldsymbol{\theta_j}$. Figure S8a combines the results for all $i=1,...,k$ and $j=1,...,n$.

Figure S8b shows the ice sheet model sea level contribution versus the LOO emulator prediction of the same quantity.

We see an overall good correlation without serious outliers. The emulator uncertainty is assessed as well in Table S2. Around 90% of the differences between emulator and ice sheet model are within the two $\sigma_\omega$ emulator uncertainty intervals, i.e. approximately as expected (95%) for a normal distribution. The emulator performance, as described above, shows no dependence on the input parameters (not shown).

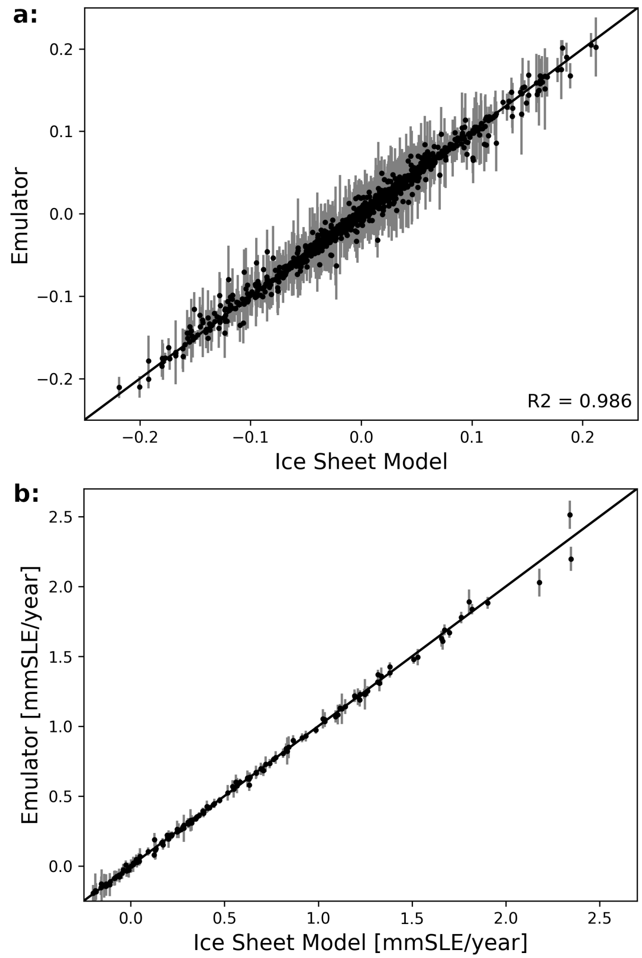


**Figure S8.** Leave-one-out emulator validation plot for year 7 (a; top) and year 50 (b; bottom). Grey error bars represent 3 $\sigma_\omega$, i.e. emulator uncertainties. All $k = 5$ PC scores of each LOO repetition are shown together in (a).

**Table S2.** Emulator validation metrics

| | Calibration | Projection |
|---|---|---|
| RMSE (predicted-simulated) | 0.007 | 0.030 mm SLE $a^{-1}$ |
| RMSE (predicted-simulated)/range | 1.65% | 1.16% |
| Pearson's r | 0.994 | 0.999 |
| Spearman's rho | 0.992 | 0.999 |
| Kendall tau | 0.938 | 0.981 |
| Fraction in 95% range | 87.7% | 87.2% |

## References

Konrad, H., Gilbert, L., Cornford, S. L., Payne, A., Hogg, A., Muir, A., and Shepherd, A.: Uneven onset and pace of ice-dynamical imbalance in the Amundsen Sea Embayment, West Antarctica, Geophysical Research Letters, 44, 910–918, https://doi.org/10.1002/2016GL070733, 2017.